Haug, Ø. T., Rosenau, M., Leever, K., Oncken, O. (2016): On the energy budgets of fragmenting rockfalls and rockslides: Insights from experiments. - *Journal of Geophysical Research*, *121*, 7, pp. 1310—1327.

DOI: http://doi.org/10.1002/2014JF003406

AGU PUBLICATIONS

JGR

Journal of Geophysical Research: Earth Surface

RESEARCH ARTICLE
10.1002/2014JF003406

Key Points:
- We study fragmenting rockslides and rockfalls using a new rock analogue material
- With an increased fragmentation, the front of the deposits travel farther, but the center of mass travels shorter
- The experimental results show that fragmentation acts as an effective energy sink

Correspondence to:
Ø. T. Haug,
o.t.haug@geo.uio.no

Citation:
Haug, Ø. T., M. Rosenau, K. Leever, and O. Oncken (2016), On the energy budgets of fragmenting rockfalls and rockslides: Insights from experiments, *J. Geophys. Res. Earth Surface*, *121*, 1310–1327, doi:10.1002/2014JF003406.

Received 6 DEC 2014
Accepted 5 JUL 2016
Accepted article online 12 JUL 2016
Published online 21 JUL 2016

On the energy budgets of fragmenting rockfalls and rockslides: Insights from experiments

Øystein Thordén Haug[1,2], Matthias Rosenau[1], Karen Leever[1], and Onno Oncken[1]

[1]GFZ German Research Centre for Geosciences, Helmholtz Centre Potsdam, Potsdam, Germany, [2]Now at Physics of Geological Processes, University of Oslo, Oslo, Norway

Abstract The travel lengths of rockfalls and rockslides can be difficult to predict due to complex interactions of numerous physical processes, such as fragmentation of the rock mass and its effect on the energy dissipation through basal and internal friction. Previous studies have shown that the front of the rockslide deposits travels farther with increased fragmentation. However, little is known about the displacement of the center of mass, which is the relevant parameter for studying the energy budget, leaving open the question whether fragmentation acts as an effective sink or source of energy. Taking advantage of a newly developed rock analogue material, we perform a total of 109 experiments to study the effect of fragmentation on the displacement of the center of mass and the energy budget of experimental rockslides. To determine the degree of fragmentation, we define a characteristic fragment size from the total mass of the experimental sample and the mass of the largest fragment. The degree of fragmentation is seen to depend linearly on the aspect ratio of the experimental sample and as a power law on its cohesion. Similar to the previous studies, our results show that the travel distance of the front of the deposits increases with the degree of fragmentation. In contrast, displacement of the center of mass is reduced with the degree of fragmentation, suggesting increased energy consumption, consistent with the assumption that fragmentation acts effectively as an energy sink.

1. Introduction

Rockfalls and rockslides can have high and unpredictable travel lengths, which makes the assessment of the hazard associated with them difficult. Of the factors that can influence their travel, fragmentation has received little attention, despite its common occurrence in both rockfalls and rockslides for a wide range of sizes [*Erismann and Abele*, 2001]. The process of fragmentation is expected to consume energy [*Locat et al.*, 2006; *Crosta et al.*, 2007], which should ultimately reduce the length of travel. Nevertheless, several studies suggest that for some very large and very far traveling rockslides, fragmentation may lead to an increased travel length [*Pollet and Schneider*, 2004; *Davies and McSaveney*, 2009; *Bowman et al.*, 2012]. This suggests a complex interplay between the fragmentation process and the other energy dissipative processes (e.g., friction), which is not yet understood.

The lack of understanding stems mainly from the lack of observations: the process of fragmentation is rarely directly observed as it occurs in nature. The current approach is, therefore, to infer kinematic and dynamic properties a posteriori from the deposits [e.g., *Pollet and Schneider*, 2004; *Locat et al.*, 2006; *Crosta et al.*, 2007; *Nocilla et al.*, 2009; *Pedrazzini et al.*, 2013]. This approach suffers from a large number of assumptions and simplifications. Recently, seismological monitoring has measured active rockfalls and slides [*Deparis et al.*, 2008; *Dammeier et al.*, 2011], making a more direct quantitative measure of rock transport kinematics and dynamics possible. However, to harvest the full potential of these observations, we need a good understanding of the processes at work. For example, by how much does the energy transferred to the ground depend on the fragmentation of a rock mass?

Rockfalls are often modeled by computing the trajectory of a single block (e.g., rockfall models of *Agliardi and Crosta* [2003]), whereas rockslides are often modeled as the flow of an assembly of particles (e.g., rock avalanche models of *Davies and McSaveney* [1999] and *Manzella and Labiouse* [2012]). Fragmentation, or any reduction of particle sizes during motion, is largely neglected. Important exceptions are the experiments of *Bowman et al.* [2012], which showed that samples could accelerate after fragmentation, causing the front of their deposits to travel further the more fragmentation they experience. Similar results were also shown in

numerical models by *Langlois et al.* [2015]. While these are illuminating studies of the kinematics of fragmenting rockslides, in order to study the energy budget of the system, one would need to consider the travel length of the center of mass rather than the front. In particular, if the center of mass also experiences an increased travel length with the degree of fragmentation, it would suggest fragmentation might effectively act as source of energy rather than the sink it is usually assumed to be.

Here we present results from experiments that aim to study some basic questions regarding the role of fragmentation in rockfalls and rockslides: (1) what controls the fragmentation process? (2) How is the travel length of the center of mass affected by the process of fragmentation? (3) How is the energy budget changed? Taking advantage of a newly developed rock analogue material [*Haug et al.*, 2014], the cohesion of which can be conveniently controlled over 2 orders of magnitude, we perform a total of 109 experiments, ensuring statistically reliable results. Notice though that our experiments do not aim to reproduce the full complexity of natural rockfalls or rockslides; they are far too simple for that. Rather, we aim to study the transport of a simple sliding system where fragmentation may occur.

In section 2, we give a brief overview of fragmentation in the framework of rockfalls and rockslides, as it is presented in the current literature. We then identify a set of controlling parameters of the process, which our new experimental setup is designed to control and monitor (section 3). The results of this study are presented in section 4, which are discussed in section 5.

2. Background

In the following, we distinguish between rockfalls and rockslides by their most dominant mode of transport [e.g., *Hungr et al.*, 2013], meaning that rockfalls are transport events dominated by free fall and the occasional impact with the ground, whereas rockslides are dominated by sliding. Yet another type are the rock avalanches, which are catastrophic rockslides produced when very large (volume $> 10^6$ m^3) rockfalls or rockslides disintegrate during motion and travel downslope at high speeds (up to 150 km/h), reaching very long distances [*Hungr et al.*, 2013].

2.1. Fragmentation in Rockfalls

In the case of rockfalls, fragmentation may occur during impacts with the ground, between periods of free fall. Therefore, it may be compared to fragmentation of an impacting brittle material, where the rapid loading cause fractures to be nucleated in different parts of the material nearly simultaneously, subsequently growing and merging (i.e., instantaneous fragmentation [*Åström*, 2006]).

Fragmentation in rockfalls is difficult to model and is largely ignored in numerical models [*Wang and Tonon*, 2010]. Instead, one often applies a coefficient of restitution that deals with both the energy lost from the impact with the ground and the energy consumed by the fragmentation process [*Bourrier et al.*, 2012]. While such models have been successful at predicting travel lengths of rockfall, comparisons between rockfall models and field tests have shown fragments to have higher velocities than predicted [*Agliardi and Crosta*, 2003]. This raises the question whether using an effective energy loss at impact is appropriate when fragmentation occurs.

2.2. Fragmentation in Rockslides and Rock Avalanches

Rockslides start out as a quasi-intact rock mass that can disintegrate during transport. Often, one separates the fragmentation into two types [*Pollet and Schneider*, 2004]. (1) A primary (static) fragmentation, where the rock mass separates by breaking rock bridges connecting fragments of more competent rock together [*Eberhardt et al.*, 2004], and (2) a dynamic fragmentation where these particles are continuously reduced in size by grinding and comminution [*Pollet and Schneider*, 2004; *Imre et al.*, 2010]. Even though this sequence of fragmentation is based on observation of rock avalanches, it is assumed here that the fragmentation of rockslides occurs in a similar manner. Even though the entire deposit of rockslides may be fragmented, zones of more intense fragmentation can be observed in localized shear zones, such as at the base of rockslides [*Pollet and Schneider*, 2004; *Imre et al.*, 2010].

Both experimental [*Bowman et al.*, 2012] and numerical models [*Langlois et al.*, 2015] have shown that fragmentation can increase the travel length of the front of rockslide deposits. The deposits of rock avalanches are highly fragmented, and fragmentation (among many other mechanisms) has been suggested to cause the long travel lengths of some rock avalanches. For example, fragmentation produces fine materials that may have a lubricating effect [e.g., *Kilburn*, 2001; *Pollet and Schneider*, 2004], or dispersive stresses from exploding

fragments may effectively reduce the normal stress at the base [e.g., *Davies and McSaveney*, 2009]. Field observations have, however, remained inconclusive: e.g., *Locat et al.* [2006] could find no clear relationship between travel lengths and the median size of fragments for a selected set of rock avalanches.

2.3. Fragmentation During Impacts

The fragmentation in the experiments presented below is driven by impacts, and we provide here a short review of fragmentation during impacts.

The deposits from brittle fragmentation during impacts are known to depend on many parameters, such as the velocity of the impact [*Kun and Herrmann*, 1999; *Timár et al.*, 2012], the geometry of the sample [*Oddershede et al.*, 1993], the initial fracture network [*Gilvarry and Bergstrom*, 1961; *Wang and Tonon*, 2010], and the angle of the impact and properties of the ground [*Wang and Tonon*, 2010]. In particular, fragmentation only occurs above thresholds of each of these variables [*Wang and Tonon*, 2010]. For example, keeping all parameters constant but the impact velocity of the samples, fragmentation occurs only above a critical velocity. This critical velocity has been linked to a continuous phase transition [*Kun and Herrmann*, 1999], where impacts below the critical velocity result in a damaged state characterized by the largest fragment being approximately of the same size as the initial sample. Impacts at velocities higher than the critical velocity result in a fragmented state, characterized by the largest fragment being much smaller than the initial sample [*Kun and Herrmann*, 1999; *Timár et al.*, 2012]. It is, however, unclear how such a phase transition is reflected by the transport and energy budget of rockfalls and rockslides.

3. Experiments

The experiments presented here are aimed at studying the process of fragmentation as it occurs during transport of materials and how it affects the transport processes. The experiments are meant to reflect this aim rather than to be downscaled replicas of natural systems. However, as fragmentation of material occurs during transport in rockfalls and rockslides, as well as rock avalanches, the experiments may provide further understanding of how the process of fragmentation affects these systems. The experiments consider only one event of fragmentation and are therefore not relevant for cases where several events occur. Also, since the experiments consider the breakup of one block into several small ones, with limited interaction after fragmentation, comminution is not expected to play any role. The experiments are therefore not relevant to study the dynamic fragmentation stage of rockslide discussed in section 2. The experiments can, perhaps, most readily provide insights into cases such as (i) the fragmentation of a block impacting on the ground, (ii) the primary fragmentation of rockslides when the quasi-intact rock disintegrates due to the accelerating movement, and (iii) in rockslides traveling over similar slope geometry as considered here and where only one event of fragmentation occurs. A more detailed discussion on the relevance of our experiments and their implications for natural systems is given in section 5.

3.1. Parameters Considered and Dimensionless Parameters

In Figure 1, the geometrical and kinematic variables considered in the experiments presented here are illustrated. The sketch shows a sample block of mass M with height h and length l elevated to a height H on a slope at angle θ. The width of the block, w, is always equal to l, and is not considered explicitly in this study. Once released, the sample slides down the slope, after which it obliquely impacts and turns around onto the horizontal plate. If fragmentation occurs, it is during this impact and subsequent turn. A key observable in our experiments is the travel distance of the center of mass, L, which is defined as the horizontal distance between the sample's center of mass at its starting point and at its final position (see Figure 1). Also measured in our experiments is the position of the front of the deposits, L_f, which is defined as the horizontal distance of the sample's initial front position and the front of the final deposits. All parameters considered in this study can be found in Table 1.

The resistance to fragmentation is determined by the cohesion, C, of the sample, which has the units of pascal and determines the material strength of the samples [*Haug et al.*, 2014]. Commonly, the degree of fragmentation is determined from the fragment size distribution (e.g., the median and average size). Unfortunately, the low cohesion of some of the samples tested in the experiments does not allow sieving of the experimental deposits without secondary fragmentation. Thus, a complete fragment size distribution is difficult to measure with confidence. Instead, similar to *Kun and Herrmann* [1999] and *Timár et al.* [2012], we characterize the degree of fragmentation of the deposits from the mass of the largest fragment, m_{max}. Further justification of this choice is given in section 4.

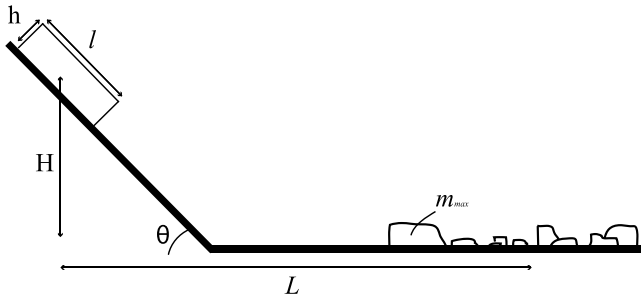

Figure 1. Sketch of the geometrical and kinematic variables considered in the experiments.

In the following, we define a set of dimensionless parameters. We start by considering the variables that are kept constant in this study. Both the angle of the plane, θ, and the angle of internal friction, ϕ, are already dimensionless and can be left as is. The last parameter to be kept constant throughout all experiments is the relative fall height of the center of mass

$$\mathcal{H} = \frac{H}{l} \tag{1}$$

Next we consider the control parameters, the first of which is the aspect ratio of the sample and characterizes its geometry.

$$\mathfrak{a} = \frac{l}{h} \tag{2}$$

An aspect ratio of 1 represents a perfect cube and in the experiments presented here varies from 2.1 to 28, which means that the samples we study always have a larger length than height. The next parameter is

$$\mathcal{F} = \frac{\rho g H}{C} \tag{3}$$

where ρ is the density of the samples before an experiment. The parameter $\mathcal{F}$ reflects the ratio between the specific potential energy and the cohesion, i.e., the ratio between the energy available and the resistance to fragmentation. For systems with small $\mathcal{F}$, cohesion dominates, suggesting that the material will not fail,

Table 1. List of Variables Considered in This Study

Variable	Form	Description
C		Cohesion of material
g		Gravitational acceleration
h		Height (thickness) of sample
H		Height of release
M		Total mass of sample
$m_{\max}$		Mass of largest fragment
l		Length of sample
L		Travel length of center of mass
L_f		Travel length of front of deposits
w		Width of sample (equal to length)
$\mathcal{L}$	L/l	The travel length of center of mass relative to its own size
$\mathcal{L}_f$	L_f/l	The travel length of deposit front relative to its own size
$\mathcal{H}$	H/l	Relative fall height compared to its own size
$\mathfrak{a}$	l/h	Aspect ratio of sample
m_c	$M/m_{\max}$	Characteristic fragment size-degree of fragmentation
$\mathcal{F}$	$\rho g H/C$	The potential energy relative to the cohesion
μ		Basal coefficient of friction
θ		Angle of slope
ϕ		Angle of internal friction

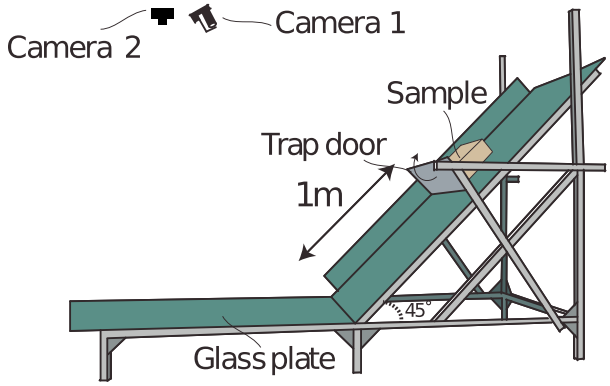

Figure 2. Drawing of the experimental setup.

whereas for systems with large $\mathcal{F}$, the potential energy dominates and fragmentation may occur. This parameter is similar to the one suggested by *Locat et al.* [2006] to determine the degree of fragmentation for natural rock avalanches. Finally, the last controlled parameter is the coefficient of basal friction, μ, which is already dimensionless.

Lastly, we consider the measured parameters. From the experiments. we measure three parameters: first is the relative travel distance of the center of mass

$$\mathcal{L} = \frac{L}{l} \tag{4}$$

which is the ratio between the travel distance and the size of the sample. Similarly, the dimensionless travel distance of the front is

$$\mathcal{L}_f = \frac{L_f}{l} \tag{5}$$

The third measured parameter is the degree of fragmentation, which we determine by normalizing the mass of the sample M by $m_{\max}$, giving

$$m_c = \frac{M}{m_{\max}}. \tag{6}$$

This characterization implicitly assumes that the largest fragment is consistent with and characterizes the entire fragment size distribution. This can only be justified as long as it is produced in the same fragmentation event as the rest of the fragments, which always is the case in our experiments. The inverse of m_c has previously been recognized as the order parameter for the phase transition (see section 2) between the damaged and the fragmented state [*Kun and Herrmann*, 1999; *Timár et al.*, 2012]. It has also been used by *Nocilla et al.* [2009] to characterize the degree of fragmentation of rockfalls. In general, m_c provides a measure for the damage the material has experienced. A value of $m_c = 1$ reflects a completely intact sample, while an increasing value reflects an increasingly fragmented deposit. In the study presented here, m_c varies between ~1 and 25.

In the end, a set of nine parameters (see bottom part of Table 1) is considered in the experiments, of which three parameters are kept constant, three are controlled and varied, and three are measured. The experiments, described below, are designed such that these parameters are controlled and monitored.

3.2. Experimental Setup

In the experiments, the opening of a trap door releases a rigid block of brittle analogue material down a slope of 45° (Figure 2). At the base of the slope, the material impacts onto a horizontal plate, undergoes fragmentation, and finally comes to rest. In each experiment, the center of mass (L), the front (L_f), and the degree of fragmentation (characterized by m_c) of the deposits are measured, the two former by image analysis (see below) and the latter by manually weighing the mass of the total sample (before the experiments) and that of the largest fragment.

Here we report on three experimental series: $\mathfrak{a}$ series, $\mathcal{F}$ series, and μ series, where the prefixes refer to the parameter varied. A detailed overview of the values of the parameters used in this study is provided in Table 2. In the $\mathfrak{a}$ series, the aspect ratio of the sliding material ($\mathfrak{a}$) is systematically varied, while $\mathcal{F}$ is kept constant at

Table 2. The Values of Parameters Tested in This Study[a]

$\mathfrak{a}$ Series	$\mathcal{F}$ Series	μ Series
	Constant Parameters	
$\mathcal{H} = 4.7$	$\mathcal{H} = 4.7$	$\mathcal{H} = 4.7$
$\theta = 45°$	$\theta = 45°$	$\theta = 45°$
$\phi = 30°$	$\phi = 30°$	$\phi = 30°$
$\mu = 0.2$	$\mu = 0.2$	$\mu = 0.55$
$\mathcal{F} = 0.74$	$\mathfrak{a} = 7.5$	$\mathfrak{a} = 7.5$
	Varied Parameters	
$\mathfrak{a} = 28$ (2)	$\mathcal{F} = 3.1$ (6)	$\mathcal{F} = 3.1$ (5)
$\mathfrak{a} = 19$ (4)	$\mathcal{F} = 0.63$ (4)	$\mathcal{F} = 0.84$ (16)
$\mathfrak{a} = 13$ (4)	$\mathcal{F} = 0.35$ (5)	$\mathcal{F} = 0, 12$ (4)
$\mathfrak{a} = 9.4$ (3)	$\mathcal{F} = 0.30$ (5)	$\mathcal{F} = 0, 035$ (6)
$\mathfrak{a} = 7.4$ (16)	$\mathcal{F} = 0.12$ (5)	
$\mathfrak{a} = 5.8$ (4)	$\mathcal{F} = 0.065$ (6)	
$\mathfrak{a} = 4.7$ (5)	$\mathcal{F} = 0.035$ (6)	
$\mathfrak{a} = 3.8$ (5)		
$\mathfrak{a} = 2.9$ (5)		
$\mathfrak{a} = 2.3$ (5)		
$\mathfrak{a} = 2.1$ (1)		

[a]The number in the parentheses gives the number of experimental runs for that value.

0.74. The aspect ratio was controlled by varying the thickness (h) of the sample, while keeping the samples' length (l) constant at 15 cm. In the $\mathcal{F}$ series, the ratio between potential energy and cohesion is varied by systematically varying the cohesion of the samples. In this series of experiments, the aspect ratio is kept constant at 7.5. In both $\mathfrak{a}$ and $\mathcal{F}$ series, both the slope and the horizontal plates are made of glass with friction against the sample (i.e., basal friction) of $\mu = 0.2$. While this coefficient of friction is much lower than what is expected in nature, this is chosen to spread the fragments as much as possible such that detection of the fragments is easier. The effect of a higher basal friction is tested in the μ series, where cohesion is again varied, but this time the base on the horizontal plate is changed to a rough rubber mat, which has a coefficient of friction of 0.55 with the sand. The two coefficients of friction reported here are determined by measuring the force required for moving samples over the respective substrate (measured by a force sensor in previous tests not reported here). The plate on the slope in this series is also glass, ensuring the same impact velocity on the horizontal plate as in the other experiments. In all the experiments, we keep constant the fall height ($H = 71$ cm), the length of the samples ($l = 15$ cm), the angle of the slope ($\theta = 45°$), and the angle of internal friction ($\phi = 30°$).

The analogue material is produced by mixing a well-sorted fluvial sand (average grain size ~300 μm) with either gypsum powder (1–5 wt %) or potato starch (0.125–1 wt %), while both materials are dry. Then, ~10 wt % water is added to the mixture and thoroughly stirred, to obtain a homogeneous mixture. The material is left to set for 2 days (gypsum) or dried in a 900 W microwave oven for 15 min (potato starch). Properties of the analogue material have been determined by triaxial and ring shear tests [*Haug et al.*, 2014]. The cohesion of the material is controlled by type (gypsum or potato starch) and the amount of cementing agent added, ranging from 3.5 ± 2.2 to 360 ± 72 kPa. Due to the low amount of cement added (<5 wt %), the angle of internal friction and the density are close to constant and equal to 30° and $1.6 \cdot 10^3$ kg/m^3, respectively.

The cement connecting the sand grains, i.e., similar to bridges between the grains, provides the cohesion of the analogue material. Fragmentation of the samples occurs by breaking these bridges. Further, fewer grains being connected by cement as well as weaker bridges likely cause the reduction of cohesion with decreased cement concentration. We hypothesize that the measure of cohesion provided here may therefore be viewed as a measure not only of the bulk strength of the sample but also of a preexisting random fracture density. However, no systematic tests have been performed to quantify and link this fracture density to the bulk cohesion.

The use of only a single block is a simplification compared to real rocks, which more often than not contain joints and preexisting weaknesses [*Charrière et al.*, 2016]. For example, should the material used in the experiments consist of a collection of blocks, the use of a single aspect ratio to determine the geometry, and its effect on the fragmentation process, may prove too simple. However, as this would increase the complexity of our experiments, we have kept them as simple as possible: by only considering one block. The effect of various collections of blocks during fragmentation of similar experiments was considered by *Bowman et al.* [2012].

It should also be pointed out that compared to natural systems, neither the geometry of the sample nor the chute may be interpreted as a direct analogue for any natural system. However, as mentioned above, the experiments are designed to achieve the best possible insight into the processes at work. Additionally, this is a common setup for the study of rockslides in experimental models [e.g., *Davies and McSaveney*, 1999; *Manzella and Labiouse*, 2012; *Imre et al.*, 2010; *Bowman et al.*, 2012], allowing a straightforward comparison of our results to previous studies in the literature.

3.3. Collection of Data From the Experiments

The experiments are monitored using two digital optical cameras placed above the slide (see Figure 2): one camera (camera 1, 3840 × 2160 pixels = 8.29 megapixels) captures the kinematics of the experiments at a frequency of 50 Hz (giving typically ∼75 images for a ∼1.5 s experiment), while the other camera (camera 2, 1806 × 3799 pixels = 6.87 megapixels) takes a still image of the final deposits. Both cameras have a pixel length of ≈500 μm, giving ∼2–3 sand grains per pixel, the minimum resolution required for image correlation. Since camera 1 captures the acceleration stage, the impact, and the flow onto the horizontal plane, its field of view is not large enough to capture the entire deposit at the end of an experiment. That is, particles at the front of the deposit may travel outside the field of view of camera 1. Thus, the two cameras were used to image the entire travel path and runout area of the experimental samples at the required resolution.

The center of mass of a fragment is estimated from its area on the image of the final deposits from camera 2. The areas of the fragments projected on the images are determined by image analysis [see *Haug et al.*, 2014]. Fragments with an area smaller than 10 pixels ($2.2 \cdot 10^{-6}$ m^2) are considered to be background (i.e., their pixels set to 0) since they cannot be properly resolved: This means that the smallest fragments considered in the analysis have cross-sectional areas of roughly 20–30 grains of sand. The center of mass for each deposit is found by the mass weighted average of position of all the fragments.

$$\mathbf{R} = \frac{1}{M'} \sum^{N} m_i' \mathbf{r_i} \tag{7}$$

where $\mathbf{R} = (x_{cm}, y_{cm})$ is the center of mass, N is the number of fragments, and $\mathbf{r_i} = (x_i, y_i)$ is the position of the center of mass of each fragment with x_i and y_i the coordinates along the width and length of the plate, respectively. The m_i' is the mass of the individual fragments found through image analysis, and the total mass M' is calculated as their sum, $M' = \sum m_i'$. Note the difference between M' and m_i', which are obtained through image analysis, and M and m_c, which are obtained by weighing the sample and the largest fragment. The travel length of the center of mass is determined by $L = y_{cm} - y_0$, where y_0 is the initial position of the center of mass.

Equation (7) requires constraints on the mass of each individual fragment, m_i, which in turn requires an estimate of their volume, where only the surface area is obtained from optical monitoring. We estimate the volume by first calculating an equivalent diameter for each fragment, given by

$$d_{eq,i} = \sqrt{\frac{4A_i'}{\pi}} \tag{8}$$

where A_i' is the area of fragment i. If $d_{eq,i} < h$, where h is the thickness of the sample, the shape of a fragment is approximated by a sphere, and the volume is given by $V_i = \frac{4}{3}\pi(\frac{1}{2}d_{eq,i})^3$. If $d_{eq,i} \geq h$, the volume is estimated to be $V_i = A_i'h$. The mass is calculated as $m_i' = V_i\rho$.

Note that the assumption that the volume of small fragments can be estimated as spheres is an approximation that does not take into consideration the real shape of the small fragments. However, the mass (volume) of each fragment is only used to determine the center of mass of the entire deposits, which is simply an average position of fragments weighted by their mass. Since most mass is concentrated in the large fragments, which is easily determined in the image analysis, the smaller fragments are expected to play a secondary role.

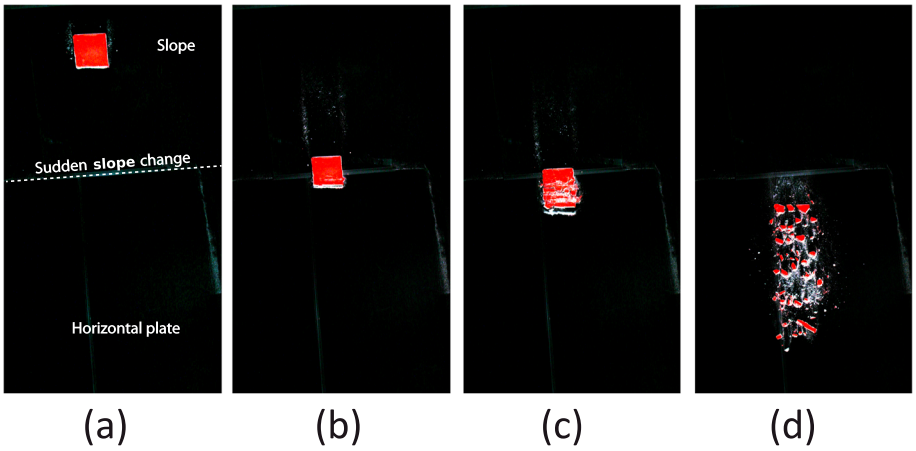

Figure 3. Sequential snapshots of an experiment with $\mathfrak{a} = 18.75$ and $\mathcal{F} = 0.74$. (a) At 0.16 s before impact, the sample slides down the slope. (b) At 0.02 s after impact, the sample fragment when impacting on the horizontal plate. (c) At 0.04 s after impact, the fragmentation occurs in sequence with the sample's travel through the corner. (d) At 0.32 s after impact, the fragments spread and slide on the horizontal plate.

Further, close observations (e.g., Figure 3) reveal that smaller fragments are close to randomly distributed within the deposits, which would reduce their contribution to the center of mass even more. The error of using such a simple shape for the small fragments is therefore not expected to be large.

To obtain the velocity of the fragments, a two-stage image analysis of the time series captured with camera 1 is performed. First, their approximate velocity is found through image correlation of two subsequent images using a Particle Image Velocimetry software (PIV strainmaster by LaVision; see *Adam et al.* [2005] for a comprehensive description). For each image, this provides a prediction where a fragment will be in the next image. Second, we binarize the time series images (from camera 1), to find the center of mass of each fragment for each time step. Then, we find the fragment that is closest to the predicted position from stage one. This allows us to recognize each fragment in two consecutive images, such that by simply considering their difference in the center of mass between the two images, a better approximation of their velocity can be achieved. Note that this approach is successful at determining velocities during simple advection but is less successful during fragmentation. In the cases where the algorithm fails to find a fragment in two consecutive images, the velocity found in step 1 is used. The velocities measured in this approach is only used for studying the kinematics during the experiments and is not used for the determination of the energy budget.

The front of each deposit is determined by the travel distance of the longest traveling fragment with a mass (m_i') larger than 1% of the total mass of the sample. The threshold of 1% is used simply to ensure the fragment to be of sufficient size and not noise from the images.

4. Results

4.1. Observations

The evolution of a typical experiment can be seen in Figure 3. The red color seen on the top of the sample is used to improve the image analysis [see *Haug et al.*, 2014]. This figure shows that the material stays intact while sliding down the slope, prior to the impact (Figure 3a). At impact (Figure 3b), the material breaks into several fragments with sizes ranging from the grain size of the sand up to a few centimeters. Closer observation of the fragmentation of the sample shows that the sample breaks apart progressively as it moves through the corner (Figures 3b and 3c). After the initial impact, a strip of fine material (i.e., sand) is observed to travel in front, followed by larger fragments (Figure 3c). After the sample has moved through the corner, the fragments slide and spread (predominantly in the downstream direction) on the horizontal plane (Figure 3d), before coming to rest.

In Figure 4, the velocities of fragments spreading on the horizontal plate of a typical experiment are presented. A gradient is observed, with high velocities in the front and low in the back. Visual inspection of the experiments (e.g., Figure 3) reveals that the fragments rarely move past each other, suggesting that the velocity gradient is not caused by segregation, i.e., by fragments with higher velocities moving to the front.

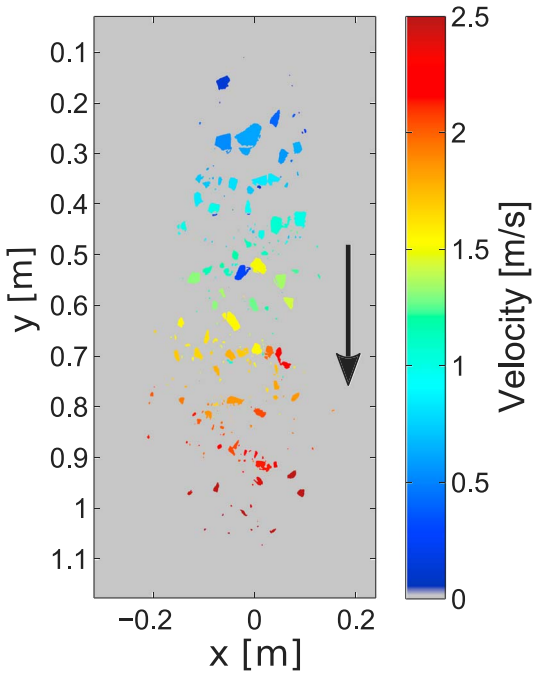

Figure 4. The velocity of fragments while they spread on the horizontal plate. The velocities are calculated using a combination of PIV and binarization of two consecutive experimental images from camera 1; the procedure of this approach is explained in section 3.3. A gradient is observed, with high velocity in the front and low in the back. The black arrow gives the dominating direction of motion. The *x* and *y* legends show the position of the fragment on the horizontal plane, where $y = 0$ is the point of the slope change.

Rather, it appears to be a direct consequence of the fragmentation process: the fragments originating from the front of the sample have the highest velocity, and the further back in the sample a fragment originates from the lower its velocity. That is, the velocity of the fragments appears to depend on the initial position of the fragment in the sample. This suggests that kinetic energy is lost progressively during the fragmentation process.

Averaged fragment size distributions (FSD) from the $\mathfrak{a}$ series, using the mass (m_i') estimated from the image analysis described above, are presented in Figure 5a. In this figure, FSDs from each experiment are calculated using 15 bins, and an average FSD is achieved by averaging each bin for experiments with the same initial conditions. In Figure 5b the inverse of the characteristic fragment mass, m_c, is plotted against the breakage parameter, Φ, used in previous studies [e.g., *Bowman et al.*, 2012; *Langlois et al.*, 2015]. The breakage is defined as

$$\Phi = \frac{S}{S_0} \tag{9}$$

where S is the area below the FSD and S_0 is the area below a FSD for the hypothetical case of a completely fragmented sample. A clear trend between these parameters is observed, which justifies the use of m_c.

The degree of fragmentation (estimated by m_c) observed in the experiments for varying aspect ratios ($\mathfrak{a}$) and potential energy to cohesion ratios ($\mathcal{F}$) is plotted in Figure 6. Here it is observed that m_c increases with both $\mathfrak{a}$ and $\mathcal{F}$. This quantifies the intuitive result that flatter blocks break easier than more cubical shapes and that weaker material fragments more than stronger materials. The degree of fragmentation appears to increase linearly with the aspect ratio (Figure 6a), and a linear regression (least squares, red line in Figure 6a, $R^2 = 0.83$) yields

$$m_c \approx 0.8\mathfrak{a} + 0.3, \quad \mathfrak{a} > 2.1 \tag{10}$$

where we specify that this linear trend is only valid for aspect ratios larger than the smallest tested here. This trend is, however, broken for the two points with largest $\mathfrak{a}$ value (colored white in Figure 6a). Several samples survived preparation, i.e., were prepared with these thicknesses (0.5–0.6 cm), but these data points represent

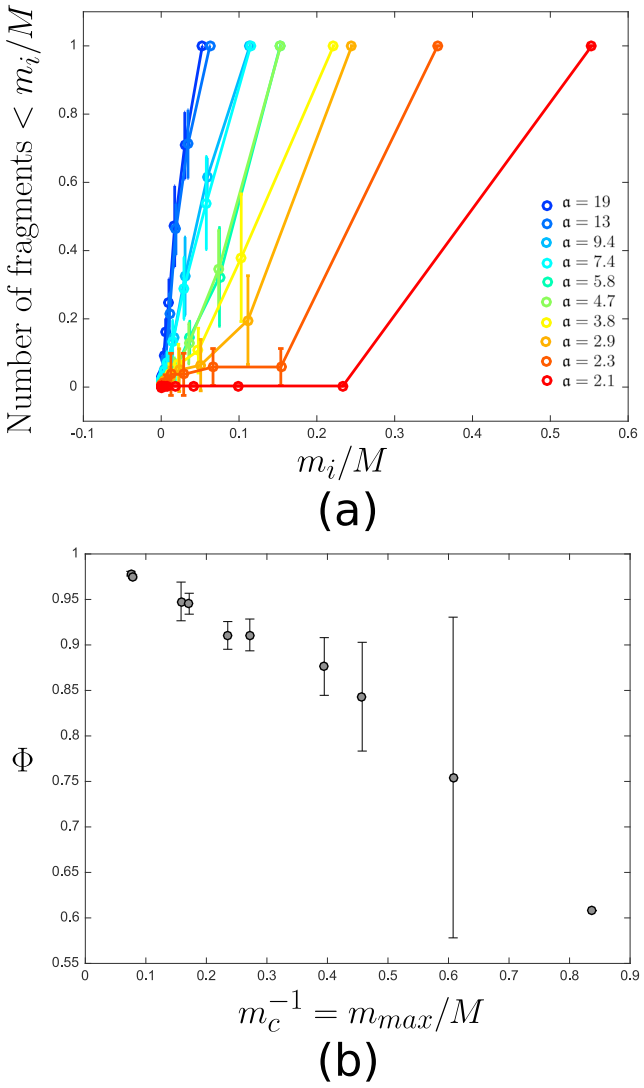

Figure 5. (a) Estimated averaged fragment size distributions for experiments from the α series. The size distributions are averaged over experiments with similar initial conditions, and the error bars are given by the standard deviation. (b) Plot of the inverse of the characteristic fragment mass, m_c, versus the breakage parameters used by previous studies (equation (9)). A clear trend is observed between these two parameters.

the only two samples that did not fail while placing them onto the chute (before the experiment started). These two points therefore reflect the limit of reasonable α values for our method and are not considered in the linear regression or in any further analysis.

The results from $\mathcal{F}$ series (Figure 6b) show a power law relationship between m_c and $\mathcal{F}$. We fit the function

$$m_c \approx 1 + \alpha \mathcal{F}^{\beta} \tag{11}$$

to the data. A best fit yields $\alpha = 6.3 \pm 0.7$ and $\beta = 0.7 \pm 0.1$ (red line in Figure 6b).

In Figure 7, the travel distance of the samples' center of mass ($\mathcal{L}$) and that of the front of the deposits ($\mathcal{L}_f$) are plotted against the degree of fragmentation (m_c), for the three series of experiments. The travel distances from both α series and $\mathcal{F}$ series are observed to collapse onto one curve. The results from the μ series, which have a higher basal friction, generally plot below the other two series of experiments. For the α series and $\mathcal{F}$ series, Figure 7a shows that as m_c increases, the travel distance decreases rapidly until m_c reaches 5–10. As m_c increases above this, a decrease of travel distance is still observed, but the difference between experiments

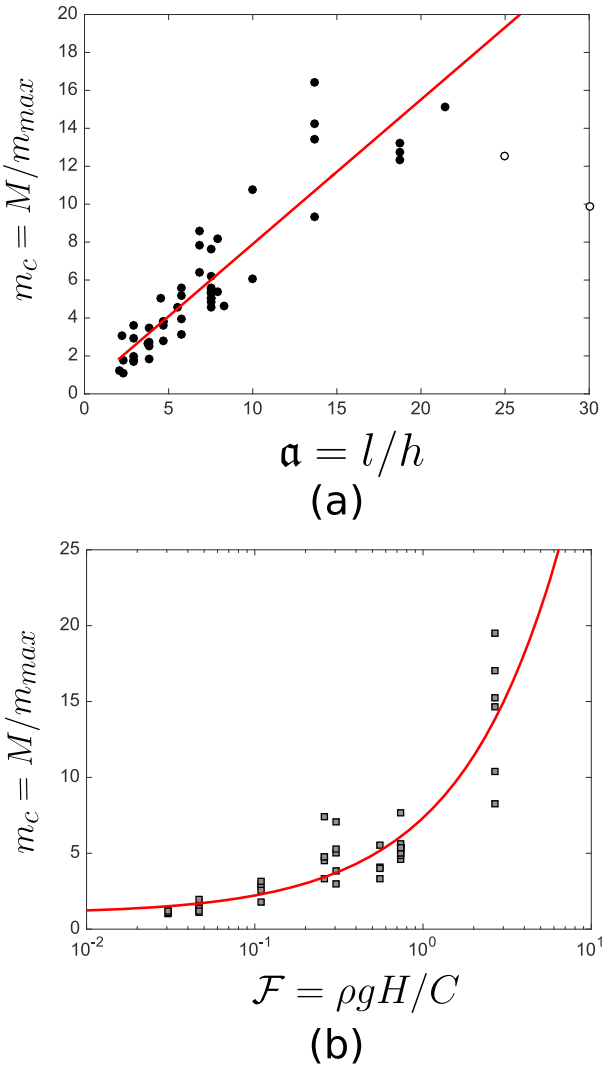

Figure 6. The degree of fragmentation, m_c, plotted against (a) the $\mathfrak{a}$ series with $\mathcal{F} = 0.74$ and (b) the $\mathcal{F}$ series with $\mathfrak{a} = 7.5$. The degree of fragmentation is observed to increase with both parameters. The red lines display the best fit lines (equations (10) (Figure 6a) and (11) (Figure 6b)); see text for details.

is less than for lower values of m_c. A similar trend is observed for μ series; however, for samples that experienced little fragmentation (open squares), the travel distance is significantly lower than experiments with $m_c = 2$–4. A detailed study of the experimental images shows that these samples experience a strong deceleration at impact, suggesting that these experiments represent a different impact mechanism than the other experiments. These points will therefore not be considered further in this study.

The collapse of the data from $\mathfrak{a}$ and $\mathcal{F}$ series means that we can treat it as one data set with regard to the travel distances of the center of mass. Based on the distribution of the points in Figure 7a, we fit

$$L \approx L_0 - L_\infty \left(1 - e^{-\gamma(m_c - 1)}\right) \tag{12}$$

where L_0 is the travel distance of the center of mass when no fragmentation occurs (i.e., $m_c = 1$), and L_∞ the one if infinite fragmentation occurs (i.e., reduced to noncohesive sand). Notice that this fitting assumes a saturation of the effect of the fragmentation on the travel distance of the center of mass. Strictly, the fitted function is only valid for the degree of fragmentation measured here. A best fit of equation (12) to the data plotted in Figure 7a yields $L_0 = 16.1 \pm 0.6$, $L_\infty = 5.8 \pm 0.9$, and $\gamma = 0.24 \pm 0.09$ for $\mathfrak{a}$ and $\mathcal{F}$ series (red line) and $L_0 = 8.36 \pm 0.38$, $L_\infty = 2.5 \pm 2.1$, and $\gamma = 0.12 \pm 0.18$ for μ series (magenta line). The difference seen in the fitting coefficients for $\mathfrak{a}$ and $\mathcal{F}$ series and μ series may possibly reflect their dependence on friction.

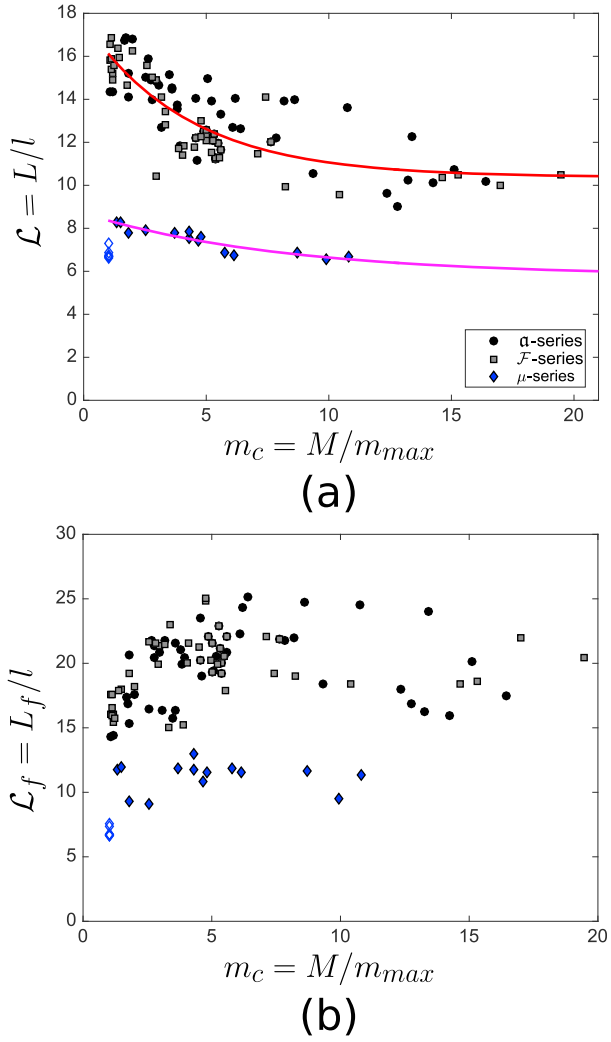

Figure 7. (a) The travel distance of the samples' center of mass plotted against the degree of fragmentation. A decrease of travel distance is observed with an increasing degree of fragmentation. The red and magenta lines display the best fit lines of equation (12) to the data; see text for details. (b) The displacement of the front of the deposits plotted against the degree of fragmentation. The front is observed to increase with the degree of fragmentation for $m_c < 5$, but for m_c above this level the front is seen to level off. The open blue diamonds represent experiments where the impact mechanisms was observed to differ from the other experiments and are not considered in any further analysis.

Unlike the center of mass, the distance traveled by the front of the samples for $\mathfrak{a}$ and $\mathcal{F}$ series shows an increase with the degree of fragmentation (Figure 7b). The front is also seen to be more strongly affected by the degree of fragmentation below $m_c \approx 5$. For degrees of fragmentation above this value, displacement of the front of the deposits is observed to saturate or even decrease. The points showing the front of the deposits for μ series do not show any clear relationship with m_c. Due to the complicated trends (increasing and saturating/decreasing for $\mathfrak{a}$ and $\mathcal{F}$ series and nonobvious for μ series), no attempt is made to fit a function to these data sets.

4.2. Determining the Energy Budget

The results in Figure 7a demonstrate that the travel distance of the center of mass depends on the degree of fragmentation, where more fragmentation leads to less far travel distances. This suggests an increased consumption of energy with fragmentation. In order to quantify this, we consider the conservation of energy of the system, which in general is given as

$$\Delta E_p = W \tag{13}$$

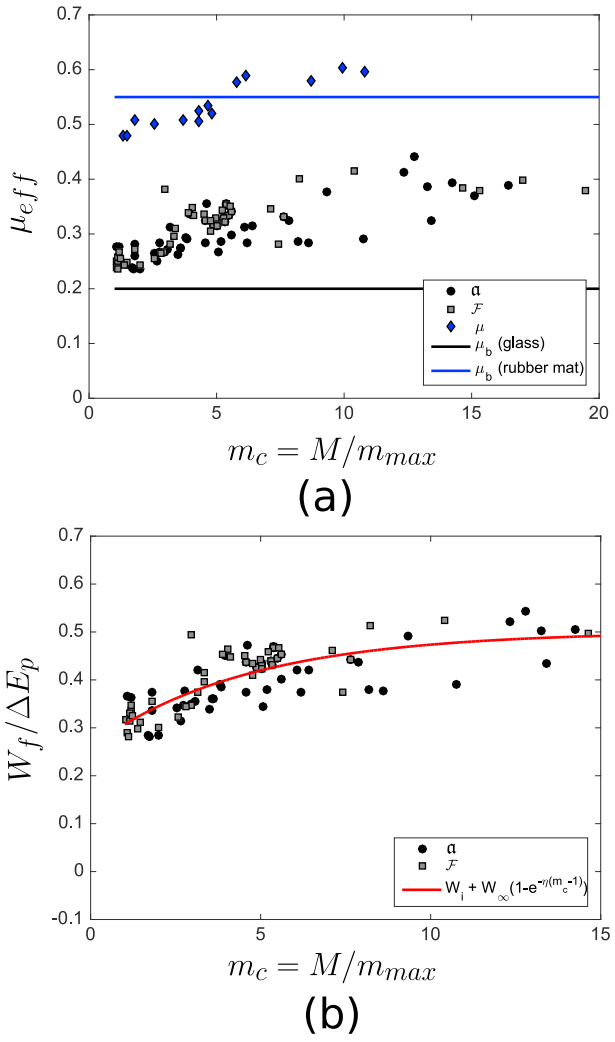

Figure 8. (a) The effective coefficient of friction plotted against the degree of fragmentation. The blue and the black lines represent the measured coefficient of basal friction. (b) The fragmentation energy plotted against the degree of fragmentation. The fragmentation energy is seen to increase for $m_c < 5$ but increases less strongly for higher degrees of fragmentation. The red line represents the best fit of equation (15).

where $\Delta E_p = MgH$, which is equal to the change of the potential energy, and W is the work done on the system over the entire period of motion. There may be several processes that contribute to the work term in equation (13). Here two approaches are considered to shed light on the energy budget of the experiments. First, we evaluate the effective basal friction coefficient, which is the friction coefficient if W only consists of work done by Coulomb friction. Second, equation (13) is solved using $W = W_\mu + W_f$, where W_μ is the work done by Coulomb friction and W_f is the sum of all other work terms, including work due to fragmentation, impacts, and internal friction.

The effective coefficient of friction on the horizontal plate is found by

$$\mu_{\text{eff}} = \frac{H - \mu_{\text{slope}} \cos\theta L_{\text{slope}}}{L_{\text{plate}}} \tag{14}$$

where L_{slope} is the length of the slope, L_{plate} is the travel length of the center of mass with respect to the base of the slope, and μ_{slope} is the friction coefficient on the slope, which is equal to 0.2 in all experiments. The effective friction as a function of the degree of fragmentation for the three series of experiments is presented in Figure 8a. In general, all experiments display an increasing effective friction with the degree of fragmentation. For $\mathfrak{a}$ and $\mathcal{F}$ series, the effective friction is always above the basal coefficient of friction on the horizontal plate ($\mu = 0.2$, black line). This is as expected since whatever the degree of fragmentation, the impact of the sample

onto the horizontal plate is expected to lead to loss of kinetic energy. In contrast, experiments in μ series with limited fragmentation display effective friction coefficients that are lower than the basal coefficient ($\mu = 0.55$, blue line). This apparent reduction in friction suggests that the assumption of a constant Coulomb friction at the base is not valid for these experiments, an assumption that is crucial for the second approach described below, and experiments from μ series are not considered there.

In the second approach, we set $W = W_\mu + W_f$, where W_μ is the work done by Coulomb friction and W_f is the sum of all other work terms, including work related to fragmentation, impacts, and internal friction. Solving equation (13) for W_f gives

$$W_f = Mg\left[H - \mu\left(L_{\text{slope}}\cos\theta + L_{\text{plate}}\right)\right]. \tag{15}$$

The values of W_f as fractions of the potential energy are plotted against the degrees of fragmentation for $\mathfrak{a}$ series and $\mathcal{F}$ series in Figure 8b. The data show that W_f/E_p increases rapidly from <30% for $m_c \sim 1$ to almost 50% for $m_c > 5$. With experiments with degrees of fragmentation higher than 5, W_f/E_p seems to saturate as m_c increases. We fit the function

$$\frac{W_f}{E_p} = W_i + W_\infty\left(1 - e^{-\eta(m_c-1)}\right) \tag{16}$$

where W_i is the fraction of the potential energy consumed when no fragmentation occurs ($m_c = 1$) and W_∞ is when $m_c \to \infty$. Similar as was mentioned above for the travel distance of the center of mass, this fitting is only valid for the degrees of fragmentation measured in this study. A best fit provides the coefficients as $W_i = 0.31 \pm 0.02$, $W_\infty = 0.19 \pm 0.03$, and $\eta = 0.22 \pm 0.09$.

5. Discussion

5.1. Controls on the Degree of Fragmentation

The results from our experiments show that the degree of fragmentation, characterized by m_c, depends linearly on the aspect ratio of the samples, i.e., their geometry (also shown by *Oddershede et al.* [1993]), and as a power law on the ratio between potential energy and cohesion (see Figure 6). For low values of these parameters ($\mathfrak{a}$ and $\mathcal{F}$), no fragmentation of the samples occurs. This suggests that a threshold for fragmentation exists, similar to that suggested by *Wang and Tonon* [2010].

5.1.1. Mechanism of Fragmentation

In the experiment presented in Figure 3, the fragmentation is observed to occur progressively as the samples move onto the horizontal plate. The observation that samples of high aspect ratios fragment easier than those with low (Figure 6a) suggests that the breakup of the samples mainly occurs by fractures propagating through the height of the sample (i.e., orthogonal to the base of the sample). Supporting this hypothesis is the shape of the large fragments, which predominantly remain with the red side up even after the end of an experiment and have the same height as the initial sample (see Figure 3). To explain these observations, we suggest that the fragmentation in the experiments occurs through tensile fractures caused by elastic bending of the samples as they are forced to turn onto the horizontal plate.

In contrast, the strip of sand preceding the larger fragments during fragmentation (see Figure 3c) appears different in that only fine material is observed. This is likely the product of the sample's impact on the horizontal plate. In this respect, localized crushing during the first impact probably causes the sand observed in the front. The localized crushing is for the most part of secondary importance compared to the elastic bending (see Figure 3).

5.2. Controls on the Travel Distance of Center of Mass

The travel distances of the samples' center of mass are seen to decrease with the degree of fragmentation (Figure 7). Further, the data from both $\mathfrak{a}$ and $\mathcal{F}$ series follow the same trend, which suggests that the degree of fragmentation is a controlling parameter for the final position of the center of mass rather than each sample's geometry or cohesion. The experiments with higher basal friction generally show less far travel distances than the experiments on glass plates but are seen to follow the same trend. These observations suggest that the travel distance in the experiments presented here is simply dependent on the degree of fragmentation and the basal friction.

Of variables not tested, the fall height, which also determines the value of $\mathcal{F}$, is expected to control the travel distance. Also, the angle of the slope, as well as the shape of the transition between the plates, can be expected

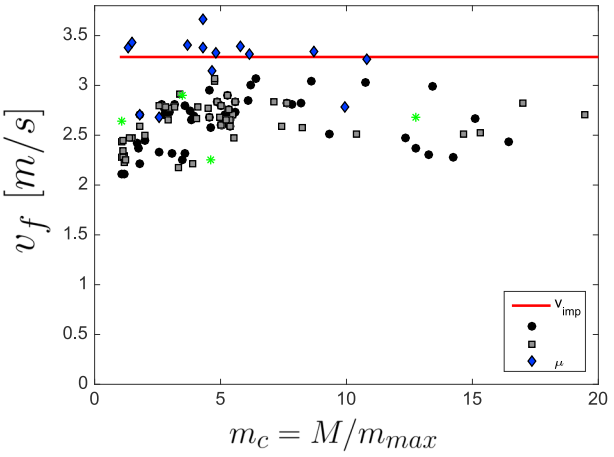

Figure 9. Estimated velocities of the fragments in the front of the deposits immediately after impact versus the degree of fragmentation. The velocities are inferred from the travel distance of the fragments (equation (17)). The red line reflects the theoretical impact speed of the sample. The green points reflect measured velocities of the front immediately after the impact; these are seen to plot within the same cloud as the estimated velocities.

to play a significant role [e.g., *Manzella and Labiouse*, 2012]. In particular, these variables not only have a direct effect on the travel length but also on the degree of fragmentation, which in turn affects the travel distance of the center of mass. Consider, for example, the case of a smooth change of angle between the slope and the horizontal plane: the granular experiments of *Manzella and Labiouse* [e.g., 2012] show that this increases the travel distance of both the center of mass and the front with respect to a sudden change of angle. However, less fragmentation can be expected in such a setup, which would likely cause a longer travel distance of the center of mass but would reduce that of the front. To be certain of these effects, in the future, systematic studies of both the fall height and the angle and its shape should be performed.

5.3. The Energy Budget

Fragmentation causes an increased spreading of the deposits (Figure 4), which leads to an increase of the position of its front with the degree of fragmentation (Figure 7b). *Bowman et al.* [2012], whose experiments are similar to ours, also recognized this. In contrast, the reduced travel distance of the center of mass shows that the energy consumption related to fragmentation increases with the degree of fragmentation (Figure 8). This is consistent with the common assumption that fragmentation acts as a sink of energy [e.g., *Crosta et al.*, 2007; *Locat et al.*, 2006].

An estimated velocity of the frontal fragments immediately after impact is presented in Figure 9, where we assume a constant basal friction such that the velocity can be inferred from their final positions using conservation of energy. That is,

$$v_f = \sqrt{2\mu g L_{\text{plate}}} \tag{17}$$

where L_{plate} is the distance from the bottom of the slope to the front of the deposit. Also plotted in this figure are velocities of the front of the sample measured by manually picking the pixels of the front for three images immediately after the impact (green points in the plot). These manually picked velocities are seen to have similar values as those estimated from equation (17) and taken as justification for using the estimated velocities. As was seen for the effective friction (Figure 8a), the assumption of a constant friction appears not to be valid for the experiments in the μ series, which display higher velocity than the impact velocity after impact. Likely, this is caused by rolling of fragments to the front of the deposits, a common occurrence in these experiments and one that would violate the assumption of constant friction. Nevertheless, this apparent increase in velocity after impact reflects an important effect of fragmentation: namely, that it can lead to a change of transport mode to a more energy-efficient one.

Considering only the experiments from the $\mathfrak{a}$ and $\mathcal{F}$ series, the velocity after impact is consistently lower than the impact velocity. Similar to *Bowman et al.* [2012], we observe an increase in velocity with fragmentation, in particular for $m_c < 5$. However, unlike *Bowman et al.* [2012], our experiments do not display acceleration after fragmentation. Possibly, this latter discrepancy can be caused by differences between the materials used.

5.3.1. Transition From Damaged to Fragmented

The travel distance of both the center of mass and front (Figure 7) is observed to depend strongly on the degree of fragmentation for $m_c < 5$ but is almost independent for m_c above this value. These results possibly reflect a continuous transition: the strong dependence on the degree of fragmentation for $1 < m_c < 5$ represents the transition between an intact but damaged block ($m_c \approx 1$) to a fragmented, granular material ($m_c \gg 1$). Possibly, these two regimes can be linked to the suggested phase transition from a damaged to fragmented state [*Kun and Herrmann*, 1999] mentioned in section 2.3. A possible implication of this is discussed below.

5.4. Implications for Natural Systems

Our experiments are simple and are not meant to model the full complexity of natural rockfalls and rockslides. The experiments aim to study the process of fragmentation in a simple sliding setting. It is worth noting, though, that the process of fragmentation may occur on all scales and in all types of transport of rocks under gravity. Therefore, despite the lack of a direct comparison between our experiments and natural systems, the process of fragmentation studied in our experiments can be relevant for a multitude of natural systems. For example, our results show that both the final position of the center of mass and the front are partly determined by the degree of fragmentation. This shows the importance of taking fragmentation into consideration when the transport of rockfalls and rockslides are studied.

5.4.1. Particular Implication for Rockfall Models

Our measurements show that the fragments have a distribution of velocities after fragmentation, with high velocity in the front and low in the back (Figure 4). Consequently, if fragmentation occurs, one must be cautious when applying a uniform reduction of velocity of the block(s) after an impact, commonly used in numerical rockfall models [*Bourrier et al.*, 2012], because it may lead to underestimation of fragment velocities. Possibly, this observation may explain the results obtained by *Agliardi and Crosta* [2003], when they compared their model results to field tests and found that the velocity of some fragments was higher than what their numerical models predicted. The consequence of the high velocity of these fragments is that fragments of the front travel farther than the other fragments (Figure 7b). This result shows how fragmentation, despite increasing energy consumption, can increase the impact a rockfall can have on a site.

5.4.2. Implications for Rockslides

As mentioned in section 3, the experiments presented here are more closely related to a primary fragmentation than to a dynamic fragmentation: our experiments study the change from a one-particle to a many-particle system. To go beyond our experiments, one can speculate that any further transport of the fragmented deposit may cause interaction between particles, likely causing comminution to take over as the dominating fragmentation mechanism, i.e., leading to the dynamic fragmentation stage. It is interesting to note that our experiments suggest saturation in energy loss for high m_c. This may suggest that an upper limit of approximately 50% of the available potential energy can be lost in the static fragmentation stage of rockslides.

Another observation, of a more indirect effect but perhaps of even greater importance, is the change of mode of transport of frontal fragments from sliding to rolling, seen for experiments in the μ series (Figure 9). This observation points to one of the most enigmatic effects of fragmentation, namely, its role in changing the dynamics of the system. These effects are, however, difficult to quantify and consider systematically, and further study of these are needed.

Our experimental results clearly show an energy loss to fragmentation. While we should be careful in directly comparing our experiments to natural prototypes, it seems fair to say that if fragmentation is to act as a source of energy in natural cases (such as discussed in section 2), it must include mechanisms that are not included in our experiments.

6. Conclusion

We have performed experiments aimed at studying the effect of fragmenting on rockslides. Our results show that the degree of fragmentation depends on the ratio between specific potential energy and cohesion ($\mathcal{F}$) as a power law, while it depends linearly on the aspect ratio of the sample ($\mathfrak{a}$). No fragmentation occurs below specific thresholds of each of these parameters. The mechanisms of fragmentation are interpreted as a combination of localized crushing during impact and elastic bending during the turn of the sample onto the horizontal plate, with the latter being the dominant one.

Similar to what previous studies have shown, the front of the deposits travel farther with increased degree of fragmentation. In contrast, the travel distance of the center of mass is seen to decrease with the degree of fragmentation. We propose an empirical scaling law that describes the travel length of the center of mass and the degree of fragmentation (equation (12)). Qualitatively, our observations imply that despite the longer reach of the front, energy consumption increases with the degree of fragmentation and is consistent with the hypothesis of fragmentation as an energy sink. Quantitatively, an empirical scaling law for the relationship between the energy lost to fragmentation and the degree of fragmentation is proposed for the experiments (equation (16)), which might be applicable to the natural prototype; however, application might involve modification and requires thorough validation.

The increased travel length of the front of the deposits is seen to be a direct consequence of the fragmentation process, which actively spreads the fragments after impact. This fragmentation-induced spreading implies that caution must be used when a single coefficient is used to account for the loss of kinetic energy after an impact.

The results of this study imply that energy consumption related to static fragmentation, such as it is seen in rockfalls and in the initial stages of rockslides and rock avalanches, can be limited to below ~50% of the available potential energy. However, our experiments show that fragmentation may introduce complexities by changing the mode of transport, e.g., from sliding to rolling, making the travel lengths less predictable.

Acknowledgments

The authors would like to thank Frank Neumann and Thomas Ziegenhagen for construction and technical assistance. The work is supported by the Helmholtz Graduate Research School GEOSIM and the German Ministry for Education and Research (BMBF, FKZ03G0809A). The authors would also like to thank Andrea Pedrazzini, Tim Davies, one anonymous reviewer, and the Editors of the *Journal of Geophysical Research-Earth Surface* for the question and comments that greatly improved this contribution. The data for this paper are available by contacting the corresponding author.

References

Adam, J., J. Urai, B. Wieneke, O. Oncken, K. Pfeiffer, N. Kukowski, J. Lohrmann, S. Hoth, W. Van Der Zee, and J. Schmatz (2005), Shear localisation and strain distribution during tectonic faulting—New insights from granular-flow experiments and high-resolution optical image correlation techniques, *J. Struct. Geology*, *27*(2), 283–301.

Agliardi, F., and G. Crosta (2003), High resolution three-dimensional numerical modelling of rockfalls, *Int. J. Rock Mech. Min. Sci.*, *40*(4), 455–471, doi:10.1016/S1365-1609(03)00021-2.

Åström, J. A. (2006), Statistical models of brittle fragmentation, *Adv. Phys.*, *55*(3–4), 247–278, doi:10.1080/00018730600731907.

Bourrier, F., F. Berger, P. Tardif, L. Dorren, and O. Hungr (2012), Rockfall rebound: Comparison of detailed field experiments and alternative modelling approaches, *Earth Surf. Processes Landforms*, *37*(6), 656–665.

Bowman, E. T., W. A. Take, K. L. Rait, and C. Hann (2012), Physical models of rock avalanche spreading behaviour with dynamic fragmentation, *Can. Geotech. J.*, *49*(4), 460–476, doi:10.1139/t2012-007.

Charriére, M., F. Humair, C. Froese, M. Jaboyedoff, A. Pedrazzini, and C. Longchamp (2016), From the source area to the deposit: Collapse, fragmentation, and propagation of the Frank Slide, *Bull. Geol. Soc. Am.*, *128*(1–2), 922–930, doi:10.1130/B31243.1.

Crosta, G. B., P. Frattini, and N. Fusi (2007), Fragmentation in the Val Pola rock avalanche, Italian Alps, *J. Geophys. Res.*, *112*, F01006, doi:10.1029/2005JF000455.

Dammeier, F., J. R. Moore, F. Haslinger, and S. Loew (2011), Characterization of alpine rockslides using statistical analysis of seismic signals, *J. Geophys. Res.*, *116*(F4), F04024, doi:10.1029/2011JF002037.

Davies, T. R., and M. J. McSaveney (1999), Runout of dry granular avalanches, *Can. Geotech. J.*, *36*(2), 313–320, doi:10.1139/t98-108.

Davies, T. R., and M. J. McSaveney (2009), The role of rock fragmentation in the motion of large landslides, *Eng. Geol.*, *109*(1–2), 67–79, doi:10.1016/j.enggeo.2008.11.004.

Deparis, J., D. Jongmans, F. Cotton, L. Baillet, F. Thouvenot, and D. Hantz (2008), Analysis of rock-fall and rock-fall avalanche seismograms in the French Alps, *B. Seismol. Soc. Am.*, *98*(4), 1781–1796, doi:10.1785/0120070082.

Eberhardt, E., D. Stead, and J. Coggan (2004), Numerical analysis of initiation and progressive failure in natural rock slopes the 1991 Randa rockslide, *Int. J. Rock Mech. Min. Sci.*, *41*(1), 69–87, doi:10.1016/S1365-1609(03)00076-5.

Erismann, T. H., and G. Abele (2001), *Dynamics of Rockslides and Rockfalls*, Springer Science & Business Media, Berlin.

Gilvarry, J., and B. Bergstrom (1961), Fracture of brittle solids. II. Distribution function for fragment size in single fracture (experimental), *J. Appl. Phys.*, *32*(3), 400–410.

Haug, Ø. T., M. Rosenau, K. Leever, and O. Oncken (2014), Modelling fragmentation in rock avalanches, *Landslide Science for a Safer Geo-Environment*, *2*, 93–100, doi:10.1007/978-3-319-05050-8_16.

Hungr, O., S. Leroueil, and L. Picarelli (2013), The Varnes classification of landslide types, an update, *Landslides*, *11*(2), 167–194, doi:10.1007/s10346-013-0436-y.

Imre, B., J. Laue, and S. M. Springman (2010), Fractal fragmentation of rocks within sturzstroms: Insight derived from physical experiments within the ETH geotechnical drum centrifuge, *Granular Matter*, *12*(3), 267–285, doi:10.1007/s10035-009-0163-1.

Kilburn, C. R. J. (2001), *The Flow of Giant Rock Landslides*edited by U. Briegel and W. J. Xiao, pp. 245–265, Elsevier, Amsterdam.

Kun, F., and H. Herrmann (1999), Transition from damage to fragmentation in collision of solids, *Phys. Rev. E: Stat. Phys. Plasmas Fluids Relat. Interdisciplin.*, *59*(3), 2623–2632, doi:10.1103/PhysRevE.59.2623.

Langlois, V. J., A. Quiquerez, and P. Allemand (2015), Collapse of a two-dimensional brittle granular column: Implications for understanding dynamic rock fragmentation in a landslide, *J. Geophys. Res.*, *120*(9), 1866–1880, doi:10.1002/2014JF003330.

Locat, P., R. Couture, S. Leroueil, J. Locat, and M. Jaboyedoff (2006), Fragmentation energy in rock avalanches, *Can. Geotech. J.*, *43*(8), 830–851, doi:10.1139/t06-045.

Manzella, I., and V. Labiouse (2012), Empirical and analytical analyses of laboratory granular flows to investigate rock avalanche propagation, *Landslides*, *10*(1), 23–36, doi:10.1007/s10346-011-0313-5.

Nocilla, N., A. Evangelista, and A. Scotto di Santolo (2009), Fragmentation during rock falls: Two Italian case studies of hard and soft rocks, *Rock Mech. Rock Eng.*, *42*(5), 815–833, doi:10.1007/s00603-008-0006-0.

Oddershede, L., P. Dimon, and J. Bohr (1993), Self-organized criticality in fragmenting, *Phys. Rev. Lett.*, *71*(19), 3107–3110.

Pedrazzini, A., M. Jaboyedoff, A. Loye, and M.-H. Derron (2013), From deep seated slope deformation to rock avalanche: Destabilization and transportation models of the Sierre landslide (Switzerland), *Tectonophysics*, *605*, 149–168.

Pollet, N., and J.-L. Schneider (2004), Dynamic disintegration processes accompanying transport of the Holocene Flims sturzstrom (Swiss Alps), *Earth Planet Sc. Lett.*, *221*(1–4), 433–448, doi:10.1016/S0012-821X(04)00071-8.

Timár, G., F. Kun, H. a. Carmona, and H. J. Herrmann (2012), Scaling laws for impact fragmentation of spherical solids, *Phys. Rev. E: Stat. Nonlinear Soft Matter Phys.*, *86*(1), 016113, doi:10.1103/PhysRevE.86.016113.

Wang, Y., and F. Tonon (2010), Discrete element modeling of rock fragmentation upon impact in rock fall analysis, *Rock Mech. Rock Eng.*, *44*(1), 23–35, doi:10.1007/s00603-010-0110-9.